



# Effects of geometry and operating conditions on hydrogen productivity of a fuel cell reformer



Jae Seong Lee, Juhyeong Seo, Ho Young Kim\*, Jaewon Chung, Sam S. Yoon

School of Mechanical Engineering, Korea University, Seoul, South Korea

## ARTICLE INFO

### Article history:

Received 15 October 2013

Received in revised form 12 February 2014

Accepted 13 February 2014

Available online 6 March 2014

### Keywords:

Geometric parameter

Operating condition

Fuel cell

Reformer

## ABSTRACT

A 250-kW fuel cell reformer was numerically simulated with a user-defined function that was designed to simultaneously model reforming and combustion reactions. The calculation domain was a simplified 3-D configuration. To investigate the effects of geometry and operating conditions on the hydrogen productivity, the combustor outlet position, fuel ratio, equivalence ratio, and steam to carbon ratio were variable parameters. The numerical results show that the flow distributions in the furnace vary with respect to the combustor outlet position. The varied flow results in temperature distributions, which predicts the nonuniform hydrogen productivity in each reactor. Measuring the temperatures at reactor centers is an effective method for predicting the hydrogen productivity because the overall reforming reaction is affected by the average reactor temperature, which can be estimated by the temperature at the reactor center. The overall results for varying the operating conditions were summarized as a table by some non-dimensional variables. By referring to the table, the proper operating conditions in similar reformer systems can be determined faster and more simply than by performing a conventional experiment.

© 2014 Elsevier Ltd. All rights reserved.

## 1. Introduction

The primary steam reforming reaction is strongly endothermic, and reactor designs are typically limited by heat transfer, rather than reaction kinetics [1]. Because the reforming process involves complex chemical reactions, heat-flow and reforming characteristics are difficult to measure experimentally. Computational modeling of the reforming process is also challenging because the reforming process includes both complex combustion and reforming reactions, which must be modeled simultaneously. Although several numerical approaches have investigated steam reformers [2–14], researchers have primarily examined the reformer system, neglecting the combined behavior of reforming and combustion reactions. These models typically consider parameters such as the steam–carbon ratio (SCR), flow rate in the reforming tube, size and shape of the reformer, and temperature and pressure at the tube inlet. Almost universally, they employed heat transfer empiricisms without solving the rate equations of the combustion reactions. Therefore, this work focuses on the effects of geometry and operating conditions on the reformer performance by

simultaneously modeling the reforming reactor and the combustion furnace while accounting for the reaction kinetics. As outlined by Xu and Froment [15], the kinetics of the steam–methane reaction was used to represent the reforming reaction, whereas an eddy-dissipation model was used to simulate the combustion reaction in the furnace [16]. Both reaction kinetics were built into the model with user-defined functions (UDFs). The results of this work provide insight into the operating conditions within the combustion furnace of a reformer, specifically 250-kW molten carbonate fuel cells and solid oxide fuel cells (MCFCs and SOFCs, respectively). The steam reformer is simulated as a 3-D system, and the simulation results are validated via experimental data. After this, the effects of the combustor outlet position and the operating conditions, such as the combustor–reactor fuel ratio, equivalence ratio, and SCR of the reformer system, are simulated and discussed.

## 2. Experiment

As shown in Fig. 1, a mixture of steam and methane gas passed through the reactors filled with a nickel-based catalyst, where the mixture was reformed. Heat was supplied from a combustion furnace that surrounds the reactors. Table 1 presents the experimental specifications, including the operating conditions and the properties of the catalyst. Mass flow controllers quantified the flow rates of methane and air. Water was delivered via a pump. For the

\* Corresponding author. Address: Department of Mechanical Engineering, Korea University, Anamdong, 5-Ga, Sungbukgu, Seoul 136-701, South Korea. Tel.: +82 2 3290 3356; fax: +82 2 3290 3752.

E-mail address: [kimhy@korea.ac.kr](mailto:kimhy@korea.ac.kr) (H.Y. Kim).

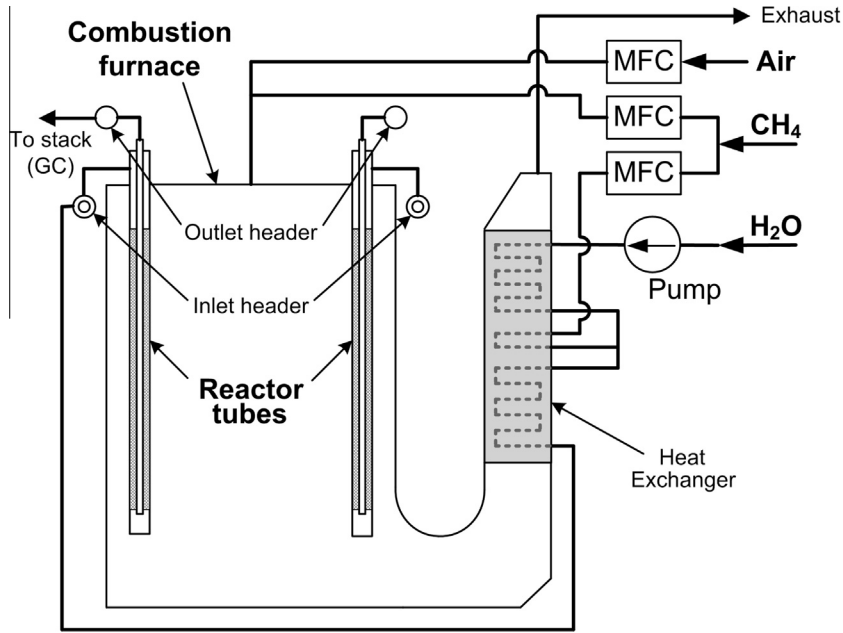


Fig. 1. Schematic of experimental apparatus of reformer for 250-kW fuel cell.

Table 1

Specifications of reformer experiment for 250-kW fuel cell.

Dimensions	
Height of furnace (m)	3.2
Width of furnace (m)	2.1
Height of catalyst zone (m)	2.0
Volume of catalyst zone (L/EA)	0.139
Number of reactors (EA)	24
Operating conditions	
Operating pressure (atm)	4
Inlet temperature of reformer (°C)	500
Flow rate of fuel to reactor (Nm <sup>3</sup> /h)	60
Flow rate of fuel to combustor (Nm <sup>3</sup> /h)	82
Catalyst properties	
Ni, Total (wt%)	>12
Shape	7 hole
Outer diameter (mm)	16
Height (mm)	11
Hole diameter (mm)	3.4
Number of holes (EA)	7

reforming reaction, methane gas and water vapor were mixed and preheated in a heat exchanger, and then supplied to the catalyst via an inlet header. The reformed gas was gathered via an outlet header and supplied to a stack of fuel cells or a gas chromatograph for composition measurements. For the combustion reaction, methane gas and air were supplied to the top of the furnace. The fuel/air mixture reacted in the combustion furnace and supplied heat to the reactor tubes and the heat exchanger.

### 3. Numerical model

A computational fluid dynamics (CFD) simulation was conducted using the commercial code, Fluent™, version 6.3.26 [17], with an appropriate UDF to simulate both the reforming and the combustion reactions. The reformer was simplified by applying symmetry and removing the headers and the heat exchanger. The calculation domain shown in Fig. 2 is a simplified version of the complex 3-D configuration. Calculations with the 3-D

configuration were performed by a double-precision, pressure-based solver under steady-state condition.

#### 3.1. Governing equations

The 3-D governing equations of the conservation of mass, momentum, and energy, as well as the species for the gas phase are given as follows:

$$\nabla \cdot (\rho \vec{v}) = 0 \quad (1)$$

$$\nabla \cdot (\rho \vec{v} \vec{v}) = -\nabla p + \nabla \cdot (\bar{\tau}) + \vec{F} \quad (2)$$

$$\nabla \cdot (\vec{v}(\rho E + p)) = \nabla \cdot (\lambda_{eff} \nabla T - \sum h_j \vec{J}_j) + S_h \quad (3)$$

$$\nabla \cdot (\rho \vec{v} Y_i) = -\nabla \cdot \vec{J}_i + R_i \quad (4)$$

where  $\vec{F}$  is the momentum source term,  $\bar{\tau}$  is the stress tensor,  $\lambda_{eff}$  is the effective conductivity,  $\vec{J}_j$  is the diffusion flux of species  $j$  (described in the next section). When the flow is turbulent, the velocities and other solution variables in the governing equations represent time-averaged values. The momentum source term,  $\vec{F}$ , includes the gravitational body force, Reynolds stresses which represent the effects of turbulences, and the external body forces of porous-media. The energy source term,  $S_h$ , is comprised of the chemical reaction heat and radiation. The species source term,  $R_i$ , represents the net rate of production of species  $i$  by the chemical reaction.

As shown in the Figs. 1 and 2, the reactor tubes which are treated as solid zones are included in the calculation domain. In the solid zones, the energy transport equation becomes the heat conduction equation as indicated in the following expression:

$$0 = \nabla \cdot (\lambda_s \nabla T) \quad (5)$$

where  $\lambda_s$  is the thermal conductivity of the solid.

The renormalization group (RNG)  $k - \varepsilon$  model was adopted for the turbulence calculations. The transport equations for the RNG  $k - \varepsilon$  model as follow:

$$\frac{\partial}{\partial x_i} (\rho k v_i) = \frac{\partial}{\partial x_j} \left( \beta_k \mu_{eff} \frac{\partial k}{\partial x_j} \right) + G_k + G_b - \rho \varepsilon_d \quad (6)$$

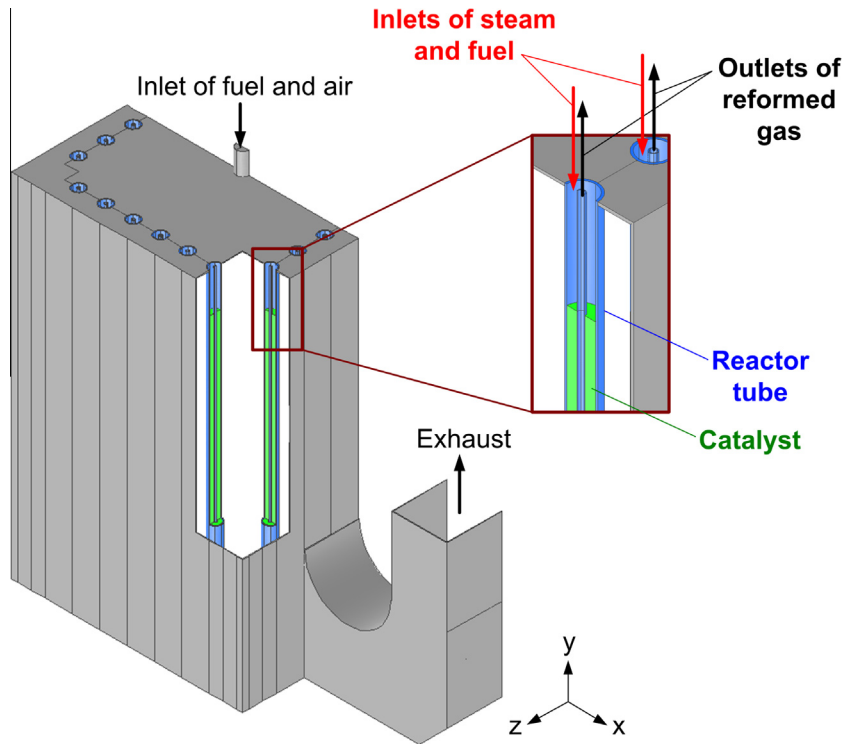


Fig. 2. Sliced and magnified views of simplified calculation domain of reformer for 250-kW fuel cell.

$$\frac{\partial}{\partial x_i} (\rho \varepsilon_d v_i) = \frac{\partial}{\partial x_j} \left( \beta_\varepsilon \mu_{eff} \frac{\partial \varepsilon_d}{\partial x_j} \right) + C_{1\varepsilon} \frac{\varepsilon_d}{k} (G_k + C_{3\varepsilon} G_b) - C_{2\varepsilon} \rho \frac{\varepsilon_d^2}{k} - R_{\varepsilon_d} \quad (7)$$

In these equations,  $G_k$  represents the generation of turbulence kinetic energy due to the mean velocity gradients,  $G_b$  is the generation of turbulence kinetic energy due to buoyancy, and  $\mu_{eff}$  is the effective viscosity. The quantities  $\beta_k$  and  $\beta_\varepsilon$  are the inverse effective Prandtl numbers for  $k$  and  $\varepsilon$ , respectively. The model constants  $C_{1\varepsilon}$  and  $C_{2\varepsilon}$ , and  $C_{3\varepsilon}$  in Eqs. (6) and (7) have values derived analytically by the RNG theory.  $R_{\varepsilon_d}$  is an additional term to make RNG model more responsive to the effects of rapid strain and streamline curvature than the standard  $k - \varepsilon$  model.

The discrete ordinates (DO) model was adopted for radiation calculation. The DO radiation model solves the radiative transfer equation (RTE) for a finite number of discrete solid angles, each associated with a vector direction fixed in the global Cartesian system. The DO model solves for as many transport equations as there are the vector directions. The solution method is identical to that used for the fluid flow and energy equations.

The treatment of the packed bed catalyst as a porous media is described in our recent study [18]. The treatment of both single species and gas mixture properties used in this study are also described in there.

### 3.2. Properties of solid materials

The components used in the experiments were made from stainless steel (SUS310S), except for the ceramic board and the catalyst. The properties of stainless steel and the ceramic board were obtained from the manufacturer specifications. The catalyst was composed of  $\text{Al}_2\text{O}_3$  and NiO, whose weight percentages were given by the manufacturer. The density, specific heat, and thermal conductivity of  $\text{Al}_2\text{O}_3$  were obtained from an online material database, MatWeb [19]. The density of NiO was also acquired from MatWeb. The specific heat of NiO was provided by Tomlinson et al. [20]. The

thermal conductivity of NiO was given by Lewis and Saunders [21]. The properties of the solid materials are listed in Table 2.

### 3.3. Reaction models

The steam–methane reforming reaction occurs on the nickel-based catalyst. The kinetic model of Xu and Froment [15] was supplied to the code as a UDF for the simulation of the reaction process. Three global reaction schemes are expressed as follows:

Reaction I:  $\text{CH}_4 + \text{H}_2\text{O} \rightarrow \text{CO} + 3\text{H}_2$  (steam–methane reforming)

Reaction II:  $\text{CO} + \text{H}_2\text{O} \rightarrow \text{CO}_2 + \text{H}_2$  (water–gas shift)

Reaction III:  $\text{CH}_4 + 2\text{H}_2\text{O} \rightarrow \text{CO}_2 + 4\text{H}_2$  (direct steam–methane reforming)

In non-premixed flames, turbulence slowly convects and mixes the fuel and oxidizer into the reaction zones where they burn quickly. In this study, a turbulence–chemistry interaction model, called the eddy-dissipation model (EDM), was used to simulate the combustion reaction. Methane combustion reaction is expressed as follows:

$\text{CH}_4 + 2\text{O}_2 \rightarrow \text{CO}_2 + 2\text{H}_2\text{O}$  (Methane combustion)

See our recent study [18] for more details about reaction models such as rate equations, coefficients, and constants of reforming and combustion reactions.

Table 2  
Properties of the solid materials.

Materials	$\rho$ (kg/m <sup>3</sup> )	$c_p$ (J/kg · K)	$\lambda$ (W/m · K)
Tube (Alloy HK40)	8000	500.0	16.0
Pipe (Alloy 800H)	7940	460.0	27.1
Catalyst	4234	829.6	38.1

### 3.4. Numerical method and boundary conditions

The governing equations were discretized using a control volume-based technique. The semi-implicit method for pressure linked equations (SIMPLE) algorithm was applied to enforce mass conservation and obtain the pressure field. The second-order upwind scheme for calculating the convective flux and the central-differencing scheme for calculating the diffusive flux were used at the control volume surface. A solution was defined to have converged when the maximum residual was less than  $10^{-3}$  and the first three significant digits of the monitoring values did not change. A no-slip condition, zero temperature gradient, and zero species-concentration gradient were specified at the wall boundaries. To calculate the radiation, the wall boundaries were treated as opaque walls [17].

## 4. Results and discussion

### 4.1. Model validation

To verify the composed UDF, the numerical results were validated with experimental results. The experimental data were selected from a literature by Lee et al. [3]. The experiment and the numerical simulation were conducted with a simple cylinder geometry. The boundary conditions and the physical parameters of the numerical simulation were equivalent to those of the experiment. The boundary conditions and the physical parameters are summarized in Table 3. Fig. 3 compares the simulation, experiment, and thermodynamics results of the dry species concentrations at the reactor outlet. The simulation result agreed well with the experimental data.

Furthermore, the UDF code was validated using the physical reformer system considered in this study. The experiment with this reformer system was conducted by Samsung Engineering Co., Ltd., and the experimental data were taken from the final report of the New and Renewable Energy Technologies Development Project of the Korea Institute of Energy Technology Evaluation and Planning [22]. Table 4 compares the experimental and numerical results of the reformer. The model with the UDFs yielded a standard deviation of 1.81%. Overall, the simulation results agreed well with the experimental data, so the code was considered appropriate for further analyses of the reformer system.

### 4.2. Effects of geometry

As shown in Fig. 2, the reformer contains reforming reactor tubes and a combustion furnace. To investigate the effects of geometry on the performance of the steam–methane reformer, the position of the combustor outlet was varied between the bottom and top of the furnace. The cases were designated by the position of the combustor outlet: at the bottom, middle, and top of the combustion furnace, respectively. Respective cases were named as Case Bottom (simply B), Case Middle (M), and Case Top (T). To determine the overall flow direction, the distributions of the

temperature and the velocity vectors were observed at a specific surface in the 3-D calculation domain. To investigate the effect of the reactor position on the hydrogen productivity, the results are summarized as plots for each reactor tube. For convenience, each reactor tube was numbered. The numbering method of the reactor tubes and the definitions of several zones are described in Fig. 4.

Fig. 5 shows that pathlines released for 8.0 s from the combustor inlets for each case where the pathlines were drawn. As shown in Fig. 5, the fuel/air mixture firstly descends to the bottom of the combustion furnace and then spreads to the sidewalls of the furnace. The figure also shows that most upward pathlines lean toward the corners of the furnace. This flow pattern is exhibited by all cases. However, the flow distributions in the upper region of the furnace are significantly different in each case. For Case B, the dominant flow is opposite the exit. For Case T, the flow opposite the exit is weak, while the dominant flow is at the corner adjacent to the exit. For Case M, the flow is relatively uniform as compared to the other cases. In Fig. 5a and b, the three pathlines exit at the outlet of the combustor. In addition, the exit times of the pathlines for Case B are shorter than those for Case M. In Fig. 5c, however, no pathline exits at the outlet of the combustor within 8 s. Because the pathlines for the first 8.0 s represent the early stage of combusted hot gas flow, Case B experiences the greatest amount of heat loss, whereas Case T experiences the smallest amount of heat loss.

In Fig. 6, the temperature contours with the velocity vectors are shown on a plane across from the reactor centers (plane at z1). For the visualization of the smaller velocity vectors, all the vectors were scaled and the vectors with velocities higher than 3 m/s were removed. As shown in Fig. 6, the distributions of the velocity vectors for each case vary. In Fig. 6a, the velocity vectors to the left of the reactor are pointed upward whereas those to the right of the reactor are pointed downward. In Fig. 6b, the velocity vectors in the upper and lower regions of the furnace are also opposite. In Fig. 6c, the velocity vectors to the left of the reactor are pointed upward until the middle of the reactor, and then, they are pointed downward from the top to the middle of the reactor. However, the velocity vectors to the right of the reactor are all pointed upward. As shown in Fig. 6, the bright region is the smallest for Case B and largest for Case T. This means that the overall temperature of the furnace is lowest for Case B and highest for Case T. This can be explained by the fact that Case B has the greatest amount of heat loss and Case T has the smallest amount of heat loss. The bright regions are located in the lower side of the furnace, which means that the upward flows from the bottom of the furnace direct hot burned gas to the middle of the furnace.

Consequently, by varying the positions of the combustor outlets, the flow distributions in the furnace are altered, resulting in different temperature distributions that predict the nonuniform hydrogen productivity in each reactor.

Fig. 7 shows some averaged values along the reactors. Fig. 7a shows the total surface heat flux, surface radiation heat flux, and reactor temperature. Fig. 7b shows the accumulations of heat fluxes. The surface at which the heat flux was calculated is the area surrounding the catalyst region, as depicted in Fig. 4. To identify the overall heat flux characteristics of the reformer, the values presented in Fig. 7 were averaged for all reactor tubes. As shown in the figure, the heat transfer from radiation is minor and the effect of the geometry on the radiation heat transfer is insignificant. The figure also shows that the reactor temperature as well as the total heat flux of Case T is higher than those of Case B. This is the same trend as that observed in the results of Figs. 5 and 6. The profiles of the total surface heat flux and the reactor temperature for Case M are the lowest among all three cases until a normalized reactor length of approximately 0.35. After that, the total heat flux of Case M is the highest among all three cases and the reactor temperature

**Table 3**  
Boundary conditions and physical parameters of UDF experiment.

<i>Boundary conditions</i>	
Inlet temperature (°C)	480
Steam–carbon ratio	3.0
GHSV ( $\text{h}^{-1}$ )	5000
<i>Physical parameters</i>	
Density of catalyst ( $\text{kg}/\text{m}^3$ )	500
Porosity	0.6
Permeability ( $\text{m}^2$ )	$2.14 \times 10^{-8}$

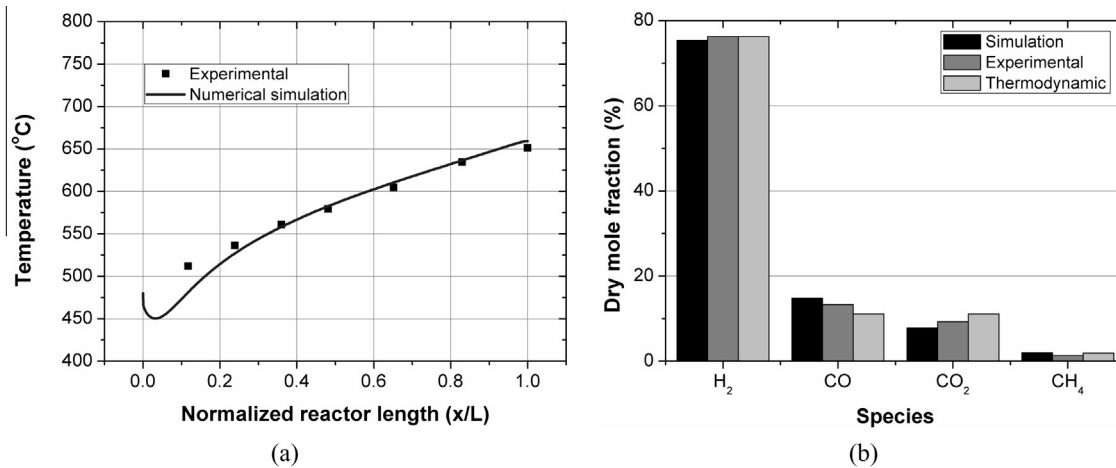


**Fig. 3.** Comparison of experimental and numerical results. (a) Temperature along reactor using optimized parameters. (b) Dry species concentrations at reactor outlet with the thermodynamic result.

**Table 4**  
Comparison of experimental and numerical results of reformer for 250-kW fuel cell.

	Experimental results	Numerical results	Deviation (%)
Dry concentration of CH <sub>4</sub> (mol%)	5.37	4.30	-1.07
Dry concentration of CO (mol%)	14.35	16.83	2.48
Dry concentration of H <sub>2</sub> (mol%)	72.98	73.19	0.21
Dry concentration of CO <sub>2</sub> (mol%)	7.26	5.67	-1.59
Standard deviation (%)			1.81

of Case M is higher than that of only Case B. At the end of the reactor, the average reactor temperature of Case M is higher by approximately 30 K than that of Case B. Referring to Fig. 6b, the upward velocity vectors from the bottom of the furnace, which is a hot region, increase until a normalized reactor length of approximately 0.35. Because convection dominates the heat transfer and the convective heat transfer is strongly influenced by the flow distributions in the furnace, it is concluded that the difference in the temperature profiles is due to the geometric variations that alter the flow distributions in the furnace.

As discussed above, because the flow in the combustion furnace is not uniform, the performance differs for each reformer tube. To investigate the effect of the positions of the tubes on the hydrogen productivity, temperatures along the all reactor tubes are presented in Fig. 8. Fig. 8a, c, and e show the temperature profiles for the front side of the reactors (i.e., reactor tubes #4–#9) whereas Fig. 8b, d, and f show the temperature profiles for the left and right side of the reactors (i.e., reactor tubes #1–#3 and #10–#12, respectively). The comparison of results of Case B between Fig. 8a and b reveals that the reactor temperatures of the front side of the reactors are lower than those of the right side of the reactors (i.e., #1–#3) and higher than those of the left side of the reactors (i.e., #10–#12). Beginning at the front side of the reactors, the reactor temperatures decrease as the measurements are taken toward the right side. This can be explained by the hot burned gas that firstly proceeds toward the left side of the furnace and then moves toward the right side of the furnace, as shown in Figs. 5a and 6a. Because the flow toward the left side of the furnace supplies some heat to the left side of the reactors, the temperature of the flow directed at the right side of the furnace decreases. Thus, the right side of the reactors receives less heat than does the left side of the

reactors. This flow characteristic yields the temperature variations among different reactors.

As shown in Fig. 8e and f, the results of Case T and B are opposite. The temperatures of the right side of the reactors are higher than those of the left side. The hot burned gas firstly proceeds toward the right side of the furnace, as shown in Figs. 5c and 6c.

As shown in Fig. 8c and d, the overall trend of Case M is similar to that of Case B. This means that the overall flow direction of Case M is also similar to that of Case B. These two cases differ in terms of the temperatures at the ends of the reactors. For Case B, the temperature variations at the ends of the reactors are greater than them for Case M. For quantitative comparison, the coefficients of variation (COV) were obtained for each case. A COV is defined as the ratio of the standard deviation to the mean. Table 5 shows COV values of some results indicating reformer performances such as average reactor temperature ( $T_{avg}$ ), fuel consumption rate ( $\gamma_{fuel}$ ), reformer efficiency for syngas ( $\eta_{syngas}$ ) and reformer efficiency for hydrogen ( $\eta_{hydrogen}$ ). The fuel conversion rate is one of the most widely used parameters for evaluating the reformer performance, and it is defined as

$$\gamma_{fuel} = \left( 1 - \frac{\dot{m}_{CH_4 @ reactor \ outlet}}{\dot{m}_{CH_4 @ reactor \ inlet}} \right) \times 100 [\%] \quad (8)$$

To express the hydrogen productivity in terms of efficiency, the thermal efficiencies for syngas and hydrogen are defined as

$$\eta_{syngas} = \frac{\dot{m}_{H_2} \times LHV_{H_2} + \dot{m}_{CO} \times LHV_{CO}}{\dot{m}_{CH_4 @ total \ fed} \times LHV_{CH_4}} \quad (9)$$

$$\eta_{hydrogen} = \frac{\dot{m}_{H_2} \times LHV_{H_2}}{\dot{m}_{CH_4 @ total \ fed} \times LHV_{CH_4}} \quad (10)$$

As shown in Table 5, The COV values are reduced more than 50% when the combustor outlet position is moved from the bottom of the furnace to the middle. Since the average temperature of the reactors are similar, this significant decrease of the COV values can be explained by the relatively uniform flow distribution of Case M. In the COV values of  $T_{avg}$ , Case T is higher than Case M. In the COV values of the other results (i.e.,  $\gamma_{fuel}$ ,  $\eta_{syngas}$ , and  $\eta_{hydrogen}$ ), however, Case T and Case M are not so different. Since Case T has higher reactor temperature than Case M, it can be concluded that the COV values of  $\eta_{syngas}$  and  $\eta_{hydrogen}$  are reduced when the reactor temperature increases and the reaction occurs sufficiently.

In Fig. 9, the results at the reactor outlets for different geometries are shown. The results are summarized as the plots

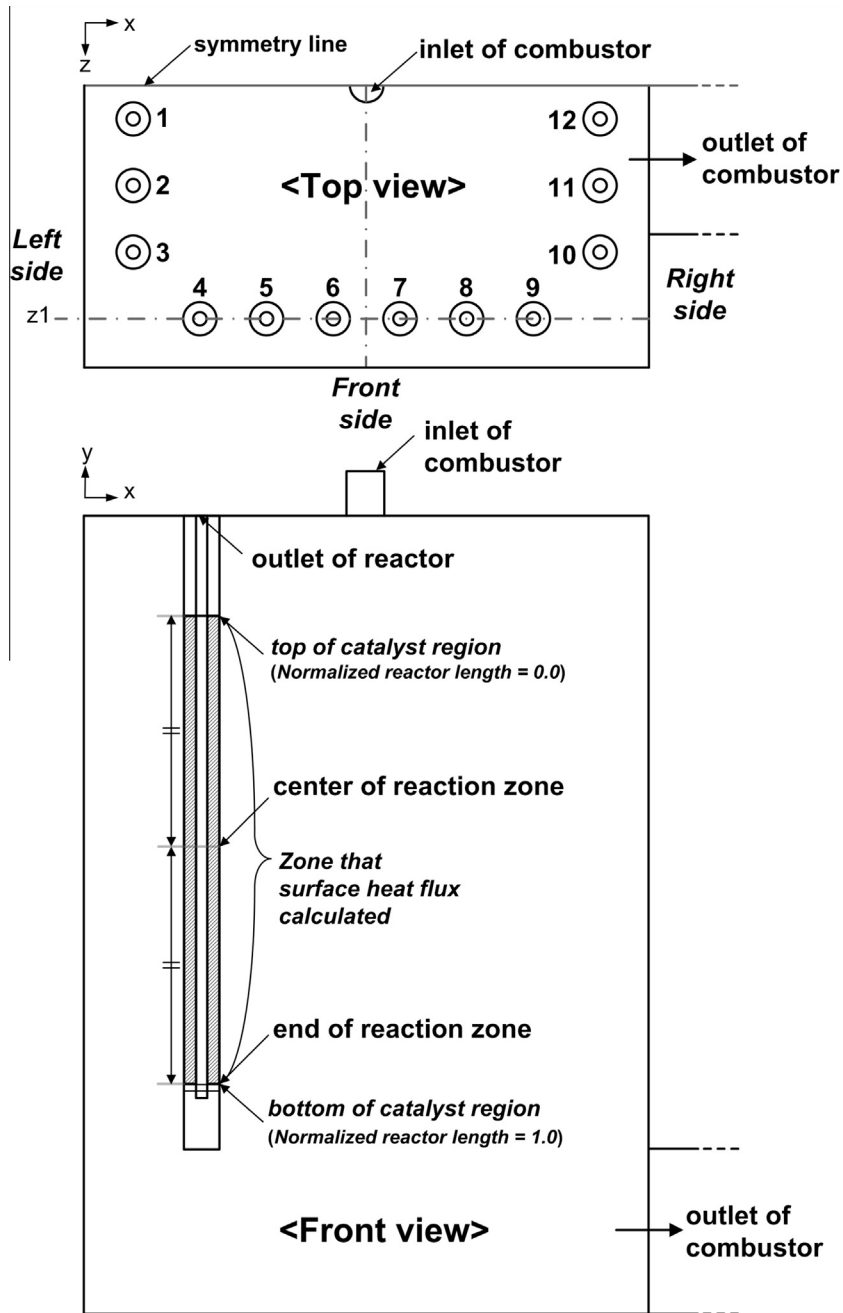


Fig. 4. Numbering method of the reactor tubes and definitions of several zones.

of temperature,  $\gamma_{\text{fuel}}$ ,  $\eta_{\text{syngas}}$ , and  $\eta_{\text{hydrogen}}$ , respectively. As shown in Fig. 9a, the outlet temperatures of Case B and Case M have similar trends (in order of reactor tube numbers: increase  $\rightarrow$  decrease  $\rightarrow$  increase). The outlet temperatures of Case T show a trend opposite to the other two cases (decrease  $\rightarrow$  increase  $\rightarrow$  decrease). The results shown in the figures represent the temperature profiles along the reactor (i.e., Fig. 8). Fig. 9a also shows that the outlet temperatures of Case B are higher than those of Case M. As shown in Fig. 9b–d, however, the higher temperature does not always indicate a higher hydrogen productivity. Although the outlet temperatures of Case M are lower than those of Case B,  $\gamma_{\text{fuel}}$ ,  $\eta_{\text{syngas}}$ , and  $\eta_{\text{hydrogen}}$  of Case M are higher than those of Case B in some reactors. Nevertheless, temperature is still an effective parameter that is easily measured and predicts the hydrogen productivity. Overall, Case T has a higher temperature than the other cases, and also

possesses a better hydrogen productivity in terms of  $\gamma_{\text{fuel}}$ ,  $\eta_{\text{syngas}}$ , and  $\eta_{\text{hydrogen}}$ .

Fig. 10 shows the average reactor temperature and temperatures measured at 3 different points. The 3 points are outlet of reactor, end and center of reaction zone (see Fig. 4). Although the temperature can be a good measurement that predicts the hydrogen productivity, the temperatures differ according to the measuring point. Among the 3 points, comparison of Fig. 9 with Fig. 10 reveals that the trends of the parameters representing the hydrogen productivity are similar to the trends of the temperatures measured at the reactor centers. In addition, the Fig. 10 shows that the profiles of the temperatures measured at reactor centers are parallel to them of the average temperatures, and therefore can be representative values of each reactor. This indicates that the overall reforming reaction is affected by the average reactor

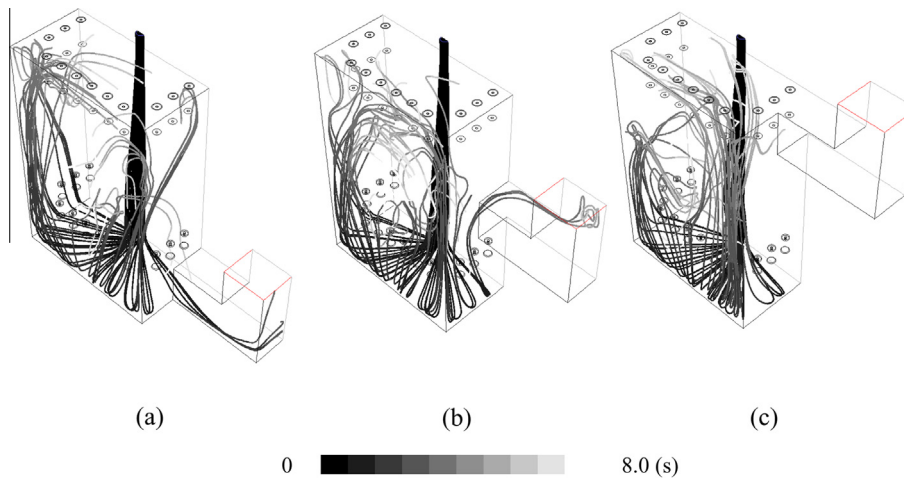


Fig. 5. Pathlines released from combustor inlets for (a) Case B, (b) Case M, and (c) Case T.

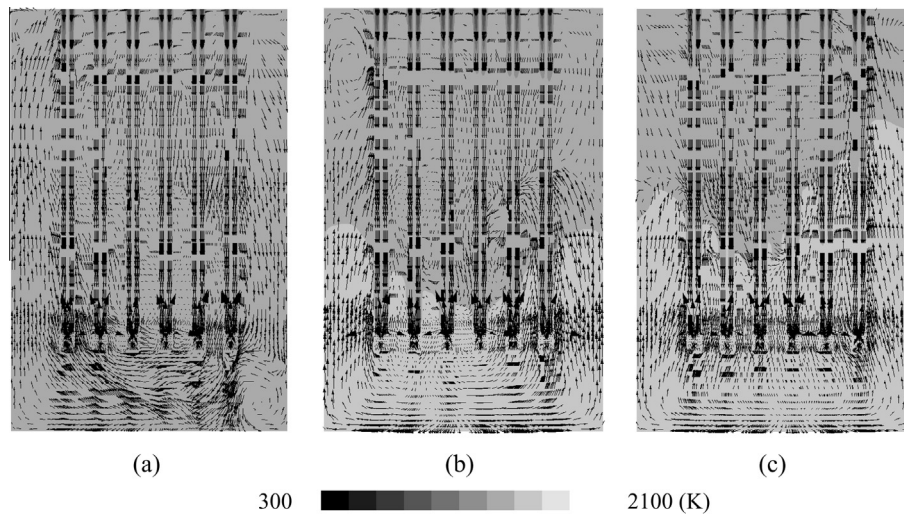


Fig. 6. Temperature contours with velocity vectors at  $z_1$  plane for (a) Case B, (b) Case M, and (c) Case T.

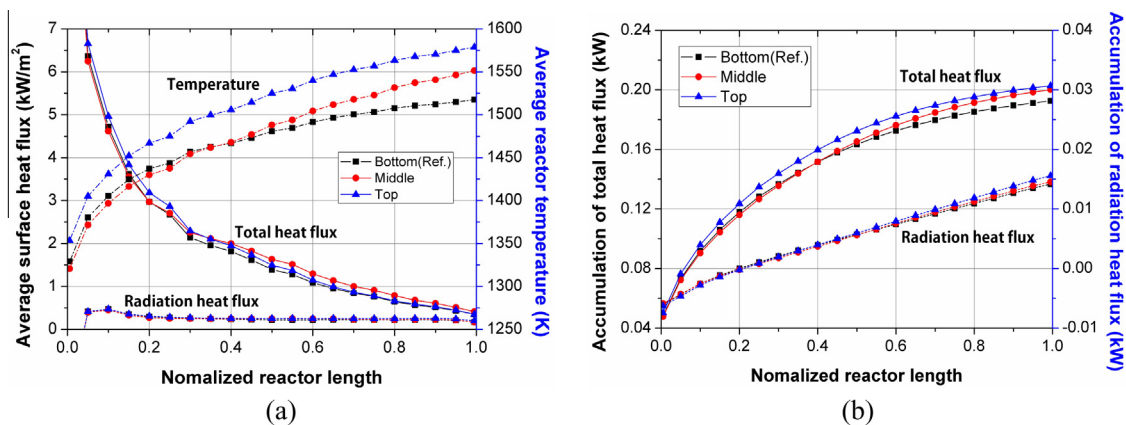


Fig. 7. Averaged values along reactor: (a) Reactor temperatures, total surface heat flux, and radiation heat flux. (b) Accumulations of total surface heat flux and radiation heat flux.

temperature. In conclusion, measuring the temperatures at the reactor centers is a more effective method for predicting the hydrogen productivity than measuring the temperatures at the reactor ends or outlets.

#### 4.3. Effects of combustor–reactor fuel ratio

In the reformer system, the selection of the operating conditions is crucial for maximizing the efficiency of the reformer. In this

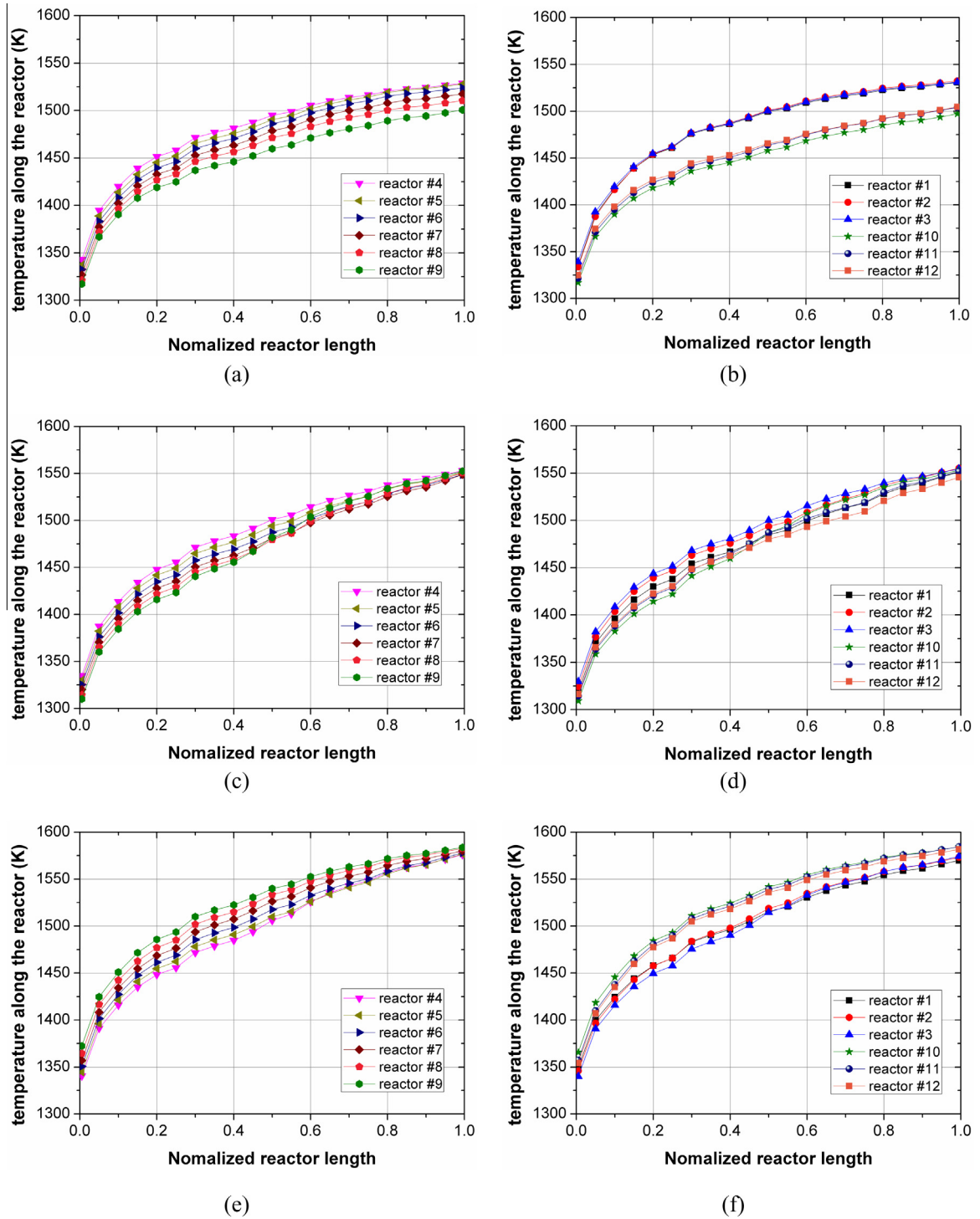


Fig. 8. Temperature profiles along reactor (a) in tubes #4–#9 for Case B, (b) in tubes #1–#3 and #10–#12 for Case B, (c) in tubes #4–#9 for Case M, (d) in tubes #1–#3 and #10–#12 for Case M, (e) in tubes #4–#9 for Case T, (f) in tubes #1–#3 and #10–#12 for Case T.

Table 5  
COV values of results that indicating reformer performances for different geometries.

COV (%)	Average reactor temperature ( $T_{avg}$ )	Fuel consumption rate ( $\dot{\gamma}_{fuel}$ )	Reformer efficiency for syngas ( $\eta_{syngas}$ )	Reformer efficiency for hydrogen ( $\eta_{hydrogen}$ )
Case bottom	0.99	0.11	0.65	0.46
Case middle	0.46	0.04	0.26	0.21
Case top	0.69	0.05	0.28	0.21

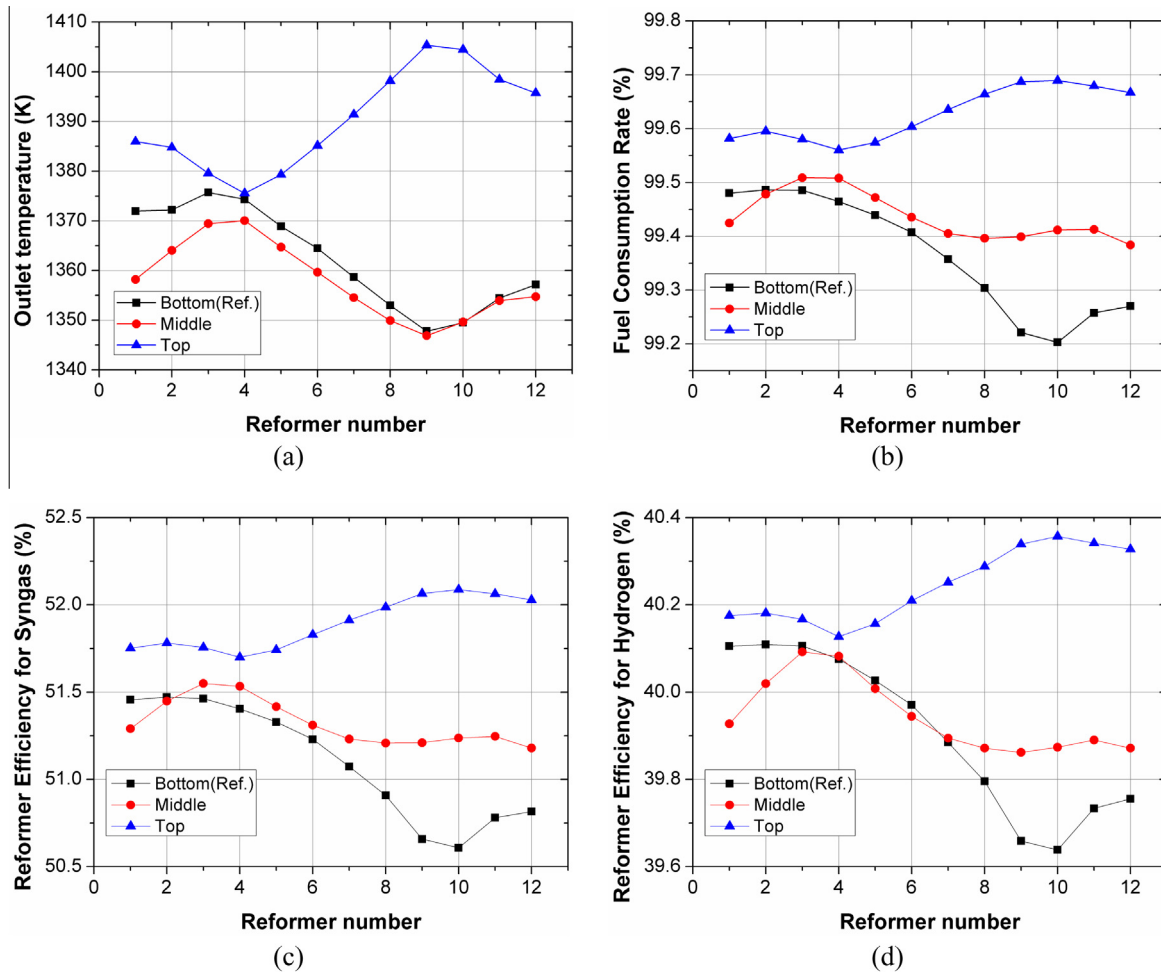


Fig. 9. The results at the reactor outlets for different geometries. (a) Outlet temperatures. (b) Fuel consumption rates. (c) Reformer  $\eta$  efficiencies for syngas. (d) Reformer efficiencies for hydrogen.

study, the fuel ratio, which is defined as the ratio of the methane flow rate in the combustor to that in the reactor, was designated as an operating parameter. This fuel ratio was varied from 40% to 140% (with 8 discrete points) by changing the methane flow rate

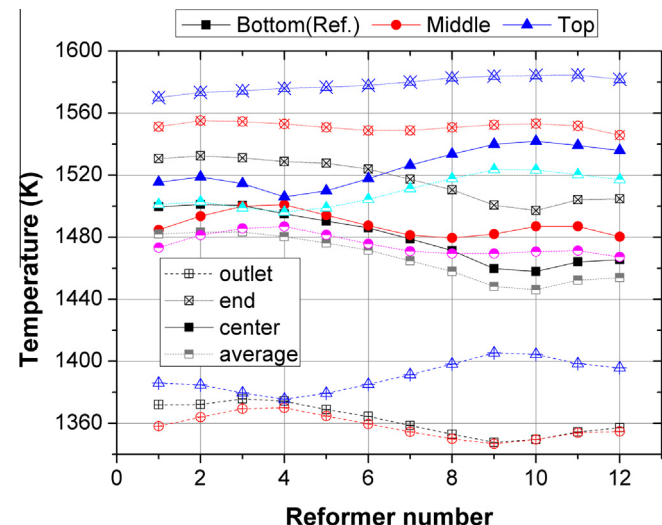


Fig. 10. Average reactor temperatures and temperatures measured at 3 different points.

of the combustor. The SCR ratio and the methane flow rate of the reactor were both fixed. The experiment was carried out at a 137% fuel ratio.

Fig. 11 shows the behavior of the system with respect to the fuel ratio. The results are summarized by plots of the reformate gas compositions, temperatures, and parameters representing the hydrogen productivity (i.e.,  $\gamma_{\text{fuel}}$ ,  $\eta_{\text{syngas}}$ , and  $\eta_{\text{hydrogen}}$ ). In Fig. 11a, it can be seen that as the fuel ratio increases, the temperature at the reactor outlet and the mole fractions of the products of MCFC and SOFC devices (i.e.,  $\text{H}_2$  and  $\text{CO}$ ) increase but the mole fractions of the reactants (i.e.,  $\text{CH}_4$  and  $\text{H}_2\text{O}$ ) decrease. As the fuel ratio increases, the temperature at the reactor outlet increases linearly. However, increasing the fuel ratio above 100% has a negligible effect on the amount of the reformed products for MCFC and SOFC devices. Fig. 11b shows that the  $\gamma_{\text{fuel}}$  increases as the fuel ratio increases. When the fuel ratio increases, the heat of combustion also increases so the methane conversion is increasingly activated. Conversely, the  $\eta_{\text{syngas}}$  and  $\eta_{\text{hydrogen}}$  are maximized when the fuel ratio is 80%. Because the reformer efficiencies have a term including the methane flow rate of the combustor, they can be decreased if the effect of increasing the fuel ratio on the syngas production is reduced. This means that a higher fuel ratio does not guarantee higher production rates. For maximum reformer efficiencies, the fuel ratio should be maintained 80%, an equivalence ratio of 1.1, and an SCR of 4. There is a disadvantage in the fuel consumption rate when lowering the fuel ratio.

4.4. Effects of combustor equivalence ratio

Because combustion is a chemical reaction between fuel and air, it is significantly affected by the composition of a fuel/air mixture. The fuel/air ( $F/A$ ) equivalence ratio is defined using a mixture composition as [23]

$$\phi = \frac{(F/A)_{actual}}{(F/A)_{stoich.}} \quad (11)$$

In our study, the equivalence ratio was adjusted from 0.4 to 1.2 (with 6 discrete points) at a fixed fuel ratio and a fixed fuel flow rate. In the experiment, the equivalence ratio was  $\phi = 1.1$  (and the fuel ratio was 137%). Fig. 12a shows that the temperature of the reactor outlet is highest at  $\phi = 1.0$ , indicative of a stoichiometric mixture. When the fuel mixture was leaner or richer than the stoichiometric fuel mixture, the reaction rates decreased. When  $\phi$  was higher than 1.0, some unburned methane exited the combustor outlet. This suggests that the temperature reduction for the richer equivalences was caused by an incomplete combustion process resulting from a shortage of an oxidizer. When  $\phi$  was less than 1.0, some unburned methane also exited the combustor outlet. This case, however, is not due to a shortage of an oxidizer, because it is a lean mixture. As  $\phi$  decreases, the air flow rate increases and so the residence time of mixture gas decreases. This lack of residence time reduces the reaction time, which results in incomplete combustion. As shown in Fig. 12b, the case of a stoichiometric mixture yielded

the largest reformer efficiencies as well as reaction rates. Thus, for maximum reformer efficiencies, the equivalence ratio must be ensured to be stoichiometric.

4.5. Effects of SCR

The SCR is the primary parameter of the reformer operation. In this study, the SCR was varied from 2.0 to 4.0 (with 5 discrete points) by fixing the mass flow rate of the reactor and combustor. The experiment was carried out at an SCR of 4.0.

Fig. 13 shows the results with respect to the SCR. The reformed gas was collected after the separation of the steam; various SCRs contain different amounts of steam. Dry mole fractions, i.e., mole fractions without the component of steam ( $H_2O$ ), were used to indicate the reformat gas compositions. As shown in Fig. 13a, the temperature at the reactor outlet decreased as the SCR decreased. Additionally, as the SCR decreased, the dry mole fractions of  $H_2$  and  $CO_2$  decreased slightly, whereas the dry mole fractions of  $CO$  and  $CH_4$  increased accordingly. This indicates that the water-gas shift (WGS) reaction that converts  $CO$  to  $CO_2$  – was increasingly activated under conditions of higher SCR. In general, the effect of the SCR variation on the reformat gas compositions is minor. As shown in Fig. 13b, the  $\gamma_{fuel}$  decreased as the SCR decreased, whereas the reformer efficiencies increased. Because the mass flow rate of the reactor was fixed, decreasing the SCR caused an increase in the methane mass flow rate, which decreased the fuel ratio. The

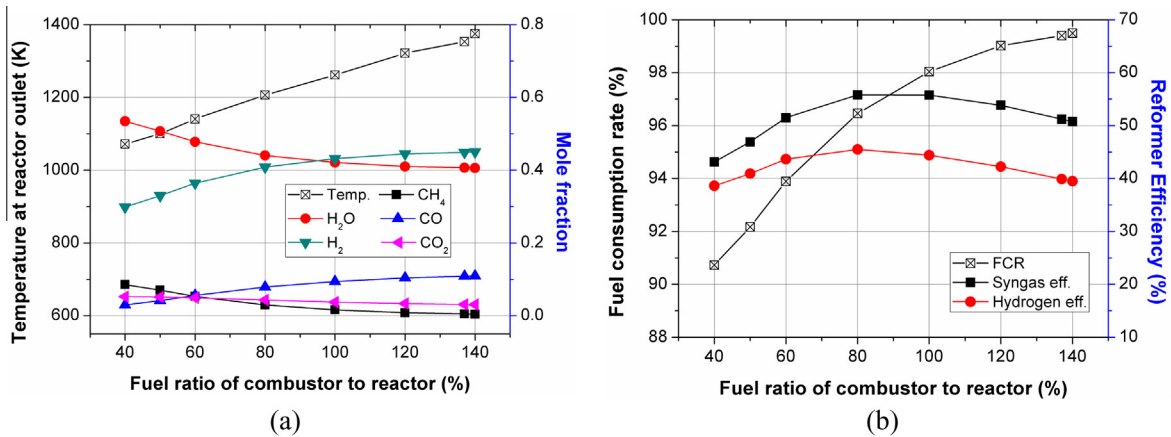


Fig. 11. The results for (a) reformat gas compositions and temperatures at reactor outlet, (b) fuel consumption rates and reformer efficiencies with respect to fuel ratio.

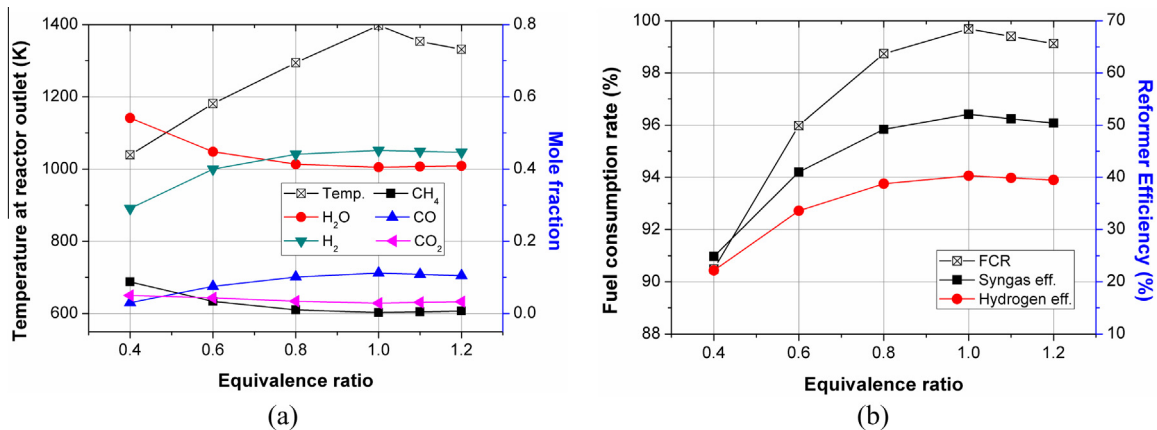


Fig. 12. The results for (a) reformat gas compositions and temperatures at reactor outlet, (b) fuel consumption rates and reformer efficiencies with respect to equivalence ratio.

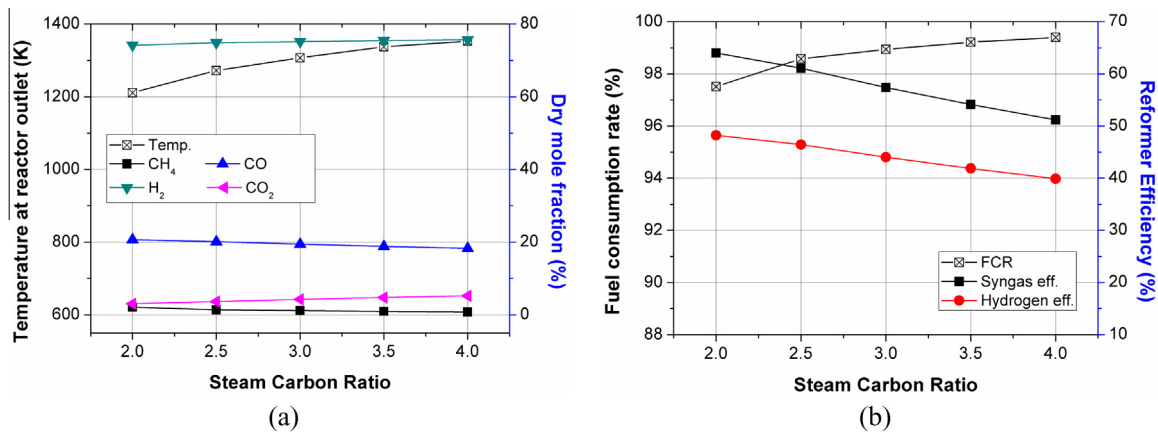


Fig. 13. The results for (a) reformat gas compositions and temperatures at reactor outlet, (b) fuel consumption rates and reformer efficiencies with respect to SCR.

Table 6

Summary of data for various operating conditions.

No.	GHSV/10 <sup>3</sup>	SCR	Fuel ratio	$\phi$	Volume ratio	$\gamma_{\text{fuel}}$	$\eta_{\text{syngas}}$	$\eta_{\text{hydrogen}}$
1	0.899	4.000	137%	1.100	41.30	99.40%	51.21%	39.89%
2	0.899	4.000	40%	1.100	41.30	90.73%	43.12%	38.61%
3	0.899	4.000	50%	1.100	41.30	92.17%	46.93%	40.94%
4	0.899	4.000	60%	1.100	41.30	93.89%	51.48%	43.65%
5	0.899	4.000	80%	1.100	41.30	96.46%	55.79%	45.50%
6	0.899	4.000	100%	1.100	41.30	98.04%	55.76%	44.41%
7	0.899	4.000	120%	1.100	41.30	99.02%	53.83%	42.24%
8	0.899	4.000	140%	1.100	41.30	99.49%	50.75%	39.50%
9	0.899	4.000	137%	0.400	41.30	90.50%	24.86%	22.17%
10	0.899	4.000	137%	0.600	41.30	95.99%	41.02%	33.58%
11	0.899	4.000	137%	0.800	41.30	98.74%	49.21%	38.77%
12	0.899	4.000	137%	1.000	41.30	99.68%	52.06%	40.31%
13	0.899	4.000	137%	1.200	41.30	99.13%	50.39%	39.48%
14	0.899	2.000	68%	1.100	41.30	97.51%	64.01%	48.24%
15	0.899	2.500	85%	1.100	41.30	98.58%	61.07%	46.45%
16	0.899	3.000	103%	1.100	41.30	98.94%	57.38%	44.03%
17	0.899	3.500	120%	1.100	41.30	99.22%	54.14%	41.88%

relevant fuel ratios of SCRs of 2, 3, and 4 were about 80%, 110%, and 140%, respectively. A comparison of Figs. 11b and 13b showed that the  $\gamma_{\text{fuel}}$ ,  $\eta_{\text{syngas}}$ , and  $\eta_{\text{hydrogen}}$  are higher when the SCR is lower under similar fuel ratio conditions. For both higher  $\gamma_{\text{fuel}}$ ,  $\eta_{\text{syngas}}$ , and  $\eta_{\text{hydrogen}}$ , it is most effective to decrease the SCR by fixing the fuel ratio. Because a lower SCR may result in the problem of carbon deposition during the operation of the reformer, the operating conditions should be properly determined.

#### 4.6. Data summary for varying operating conditions

The overall results for varying the operating conditions can be summarized by five variables. Three of the variables are the parameters in the case study: fuel ratio, equivalence ratio, and SCR. The other two are the gas hourly space velocity (GHSV) and a volume ratio. The GHSV is a type of characteristic time and is defined as the ratio of the volumetric flow rate of the reactor to the reactor volume (i.e.,  $V_{\text{reactor}}/V_{\text{reactor}}$ ). The volume ratio is defined as the ratio of the combustor volume to the reactor volume (i.e.,  $V_{\text{combustor}}/V_{\text{reactor}}$ ) which specifies the scale of difference between the combustor and the reactor. The main output results, which represent the hydrogen productivity, were selected to be the  $\gamma_{\text{fuel}}$ ,  $\eta_{\text{syngas}}$ , and  $\eta_{\text{hydrogen}}$ . The summarized results are shown in Table 6. By referring to the table, the proper operating conditions in similar reformer systems can be determined faster and more simply than by performing a conventional experiment.

## 5. Conclusions

A 250-kW fuel cell reformer was numerically simulated with a UDF that is composed for simultaneously modeling reforming and combustion reactions. The calculation domain was a simplified 3-D configuration. For the purpose of validation, the numerical results were compared with experimental data. To investigate the effects of geometry and operating conditions on the hydrogen productivity, the position of the combustor outlet, fuel ratio, equivalence ratio, and SCR were considered as variable parameters.

The numerical results show that the positions of the combustor outlets affect the flow distributions in the furnace, resulting in different temperature distributions, which predict the nonuniform hydrogen productivity in each reactor. The flow distribution and the COVs of the reformer performances were the most uniform for the case in which the combustor outlet is located at the middle of the furnace. This indicates that a uniform flow distribution in the furnace yields uniform reactor performances. Although the higher temperature does not always result in a higher hydrogen productivity, the temperature is still an effective parameter that is easily measured and predicts the hydrogen productivity. Moreover, measuring the temperatures at reactor centers is an effective method for predicting the hydrogen productivity because the overall reforming reaction is affected by the average reactor temperature, which can be estimated by the temperature at the reactor center.

The numerical results also show that a higher fuel ratio does not guarantee higher production rates, although it does enhance the

fuel consumption rate. For maximum reformer efficiency, the fuel ratio should be maintained at 80% with an equivalence ratio of 1.1 and an SCR of 4.0. There is a disadvantage in the fuel consumption rate when lowering the fuel ratio. The hydrogen productivity, including the fuel consumption rate and the reformer efficiency, are highest at  $\phi = 1.0$ , which is indicative of a stoichiometric mixture at a fuel ratio of 137% and an SCR of 4.0. When the fuel mixture was leaner or richer in oxidizers than was the stoichiometric fuel mixture, the performances degraded. For both a higher fuel consumption rate and higher reformer efficiencies, decreasing the SCR ratio by fixing the fuel ratio is effective. However, the operating conditions should be properly determined to avoid the problem of carbon deposition during the operation of the reformer.

The overall results for varying the operating conditions are summarized as a table with respect to the variable parameters. The proper operating conditions in similar reformer systems can be determined more quickly and easily via the table than by performing a conventional experiment.

### Acknowledgements

This research was supported by a Korea University Grant and the New and Renewable Energy Technologies Development Project of Korea Institute of Energy Technology Evaluation and Planning. The experiment was conducted by Samsung Engineering Co., Ltd.

### References

- [1] S. Ahmed, R. Kumar, M. Krumplet, Fuel processing for fuel cell power systems, *Fuel Cells Bull.* (1999) 4–7.
- [2] D.L. Hoang, S.H. Chan, O.L. Ding, Kinetic and modelling study of methane steam reforming over sulfide nickel catalyst on a gamma alumina support, *Chem. Eng. J.* 112 (2005) 1–11.
- [3] S. Lee, J. Bae, S. Lim, J. Park, Improved configuration of supported nickel catalysts in a steam reformer for effective hydrogen production from methane, *J. Power Sources* 180 (1) (2008) 506–515.
- [4] J. Pina, N.S. Schbib, V. Bucala, D.O. Borio, Influence of the heat-flux profiles on the operation of primary steam reformers, *Ind. Eng. Chem. Res.* 40 (23) (2001) 5215–5221.
- [5] M.N. Pedenera, J. Pina, D.O. Borio, V. Bucala, Use of a heterogeneous two-dimensional model to improve the primary steam reformer performance, *Chem. Eng. J.* 94 (1) (2003) 29–40.
- [6] M. de Jong, A.H.M.E. Reinders, J.B.W. Kok, G. Westendorp, Optimizing a steam-methane reformer for hydrogen production, *Int. J. Hydrogen Energy* 34 (1) (2009) 285–292.
- [7] H.M. Kvamsdal, H.F. Svendsen, T. Hertzberg, O. Olsvik, Dynamic simulation and optimization of a catalytic steam reformer, *Chem. Eng. Sci.* 54 (13–14) (1999) 2697–2706.
- [8] C.V.S. Murty, M.V.K. Murthy, Modeling and simulation of a top-fired reformer, *Ind. Eng. Chem. Res.* 27 (10) (1988) 1832–1840.
- [9] J. Shayegan, M.M.Y.M. Hashemi, K. Vakhshouri, Operation of an industrial steam reformer under severe condition: a simulation study, *Can. J. Chem. Eng.* 86 (4) (2008) 747–755.
- [10] D.A. Latham, K.B. McAuley, B.A. Peppley, T.M. Raybold, Mathematical modeling of an industrial steam-methane reformer for on-line deployment, *Fuel Process. Technol.* 92 (8) (2011) 1574–1586.
- [11] G. Brus, J. Szymid, Numerical modelling of radiative heat transfer in an internal indirect reforming-type SOFC, *J. Power Sources* 181 (1) (2008) 8–16.
- [12] S. Grevskott, T. Rusten, M. Hillestad, E. Edwin, O. Olsvik, Modelling and simulation of a steam reforming tube with furnace, *Chem. Eng. Sci.* 56 (2) (2001) 597–603.
- [13] Y.S. Seo, D.J. Seo, Y.T. Seo, W.L. Yoon, Investigation of the characteristics of a compact steam reformer integrated with a water-gas shift reactor, *J. Power Sources* 161 (2) (2006) 1208–1216.
- [14] J. Park, J. Bae, Numerical analysis of a steam reformer coupled with a combustion burner, *J. Fuel Cell Sci. Technol.* 7 (6) (2010) 064501-1-6.
- [15] J. Xu, G.F. Froment, Methane steam reforming methanation and water-gas shift-I intrinsic kinetics, *AIChE J.* 35 (1) (1989) 88–96.
- [16] B.F. Magnussen, B.H. Hjertager, On mathematical modeling of turbulent combustion with special emphasis on soot formation and combustion, *Symp. (Int.) Combust.* 16 (1) (1977) 719–729.
- [17] *Fluent™ v6.3.26 User Guide*.
- [18] J.S. Lee, J. Seo, H.Y. Kim, J.T. Chung, S.S. Yoon, Effects of combustion parameters on reforming performance of a steam-methane reformer, *Fuel* 111 (2013) 461–471.
- [19] MatWeb, <<http://www.matweb.com/search/PropertySearch.aspx>>, 2013 (accessed 25.07.13).
- [20] J.R. Tomlinson, L. Domash, R.G. Hay, C.W. Montgomery, The high temperature heat content of nickel oxide, *J. Am. Chem. Soc.* 77 (4) (1995) 909–910.
- [21] F.B. Lewis, N.H. Saunders, The thermal conductivity of NiO and CoO at the Neel temperature, *J. Phys. C: Solid State Phys.* 6 (15) (1973) 2525–2532.
- [22] Samsung SDI, Samsung Engineering, KIER, Korea Univ., KAIST, Development of 25-kW SOFC stack module using circular cell, Final Report, New and Renewable Energy Technologies Development Project, Korea Institute of Energy Technology Evaluation and Planning, Project no. 2008NFC12J032200, 2012.
- [23] J.B. Heywood, Internal combustion engine fundamentals, International ed., McGraw-Hill, Singapore, 1988, pp. 71–72.